Title
X-ray linear dichroic ptychography

Journal
Proceedings of the National Academy of Sciences of the United States of America, 118(3)

ISSN
0027-8424

Authors
Lo, Yuan Hung
Zhou, Jihan
Rana, Arjun
et al.

Publication Date
2021-01-19

DOI
10.1073/pnas.2019068118

Peer reviewed

X-ray linear dichroic ptychography

Yuan Hung Lo[a,b,c,d], Jihan Zhou[a,b,c], Arjun Rana[a,b,c], Drew Morrill[b,e,f], Christian Gentry[b,e,f], Bjoern Enders[g], Young-Sang Yu[h], Chang-Yu Sun[i], David A. Shapiro[h], Roger W. Falcone[b,h,j], Henry C. Kapteyn[b,e,f], Margaret M. Murnane[b,e,f], Pupa U. P. A. Gilbert[i,k,l,m,n], and Jianwei Miao[a,b,c,1]

[a]Department of Physics and Astronomy, University of California, Los Angeles, CA 90095; [b]STROBE NSF Science and Technology Center, University of Colorado Boulder, Boulder, CO 80309; [c]California NanoSystems Institute, University of California, Los Angeles, CA 90095; [d]Department of Bioengineering, University of California, Los Angeles, CA 90095; [e]JILA, University of Colorado Boulder and National Institute of Standards and Technology, Boulder, CO 80309; [f]Department of Physics, University of Colorado Boulder, Boulder, CO 80309; [g]National Energy Research Scientific Computing Center, Lawrence Berkeley National Laboratory, Berkeley, CA 94720 [h]Advanced Light Source, Lawrence Berkeley National Laboratory, Berkeley, CA 94720; [i]Department of Physics, University of Wisconsin, Madison, WI 53706; [j]Department of Physics, University of California, Berkeley, CA, 94720; [k]Department of Chemistry, University of Wisconsin, Madison, WI 53706; [l]Department of Materials Science and Engineering, University of Wisconsin, Madison, WI 53706; [m]Department of Geoscience, University of Wisconsin, Madison, WI 53706; and [n]Chemical Sciences Division, Lawrence Berkeley National Laboratory, Berkeley, CA 94720

Edited by David A. Weitz, Harvard University, Cambridge, MA, and approved November 28, 2020 (received for review September 9, 2020)

Biominerals such as seashells, coral skeletons, bone, and tooth enamel are optically anisotropic crystalline materials with unique nanoscale and microscale organization that translates into exceptional macroscopic mechanical properties, providing inspiration for engineering new and superior biomimetic structures. Using *Seriatopora aculeata* coral skeleton as a model, here, we experimentally demonstrate X-ray linear dichroic ptychography and map the *c*-axis orientations of the aragonite ($CaCO_3$) crystals. Linear dichroic phase imaging at the oxygen K-edge energy shows strong polarization-dependent contrast and reveals the presence of both narrow (<35°) and wide (>35°) *c*-axis angular spread in the coral samples. These X-ray ptychography results are corroborated by four-dimensional (4D) scanning transmission electron microscopy (STEM) on the same samples. Evidence of co-oriented, but disconnected, corallite subdomains indicates jagged crystal boundaries consistent with formation by amorphous nanoparticle attachment. We expect that the combination of X-ray linear dichroic ptychography and 4D STEM could be an important multimodal tool to study nano-crystallites, interfaces, nucleation, and mineral growth of optically anisotropic materials at multiple length scales.

coherent diffractive imaging | ptychography | X-ray linear dichroism | biominerals | 4D scanning transmission electron microscopy

Humans have been using biogenic materials as tools since the dawn of humanity. Biominerals such as bone, teeth, seashells, and coral skeletons exhibit remarkable mechanical properties and complex hierarchical organization (1). Due to these unique characteristics, biominerals often outperform their geologic or synthetic inorganic counterparts, thus attracting significant interest in understanding the mechanisms of the biologically controlled mineralization processes for modern nanotechnology (2). Careful understanding of the three-dimensional (3D) arrangement of biominerals has important engineering implications and has led to bioinspired materials that outperform nonbiomimetic, inorganic synthetic analogs (3).

One of the most common natural biominerals is calcium carbonate ($CaCO_3$), which occurs in bacteria, algae, marine organisms, and humans (4). $CaCO_3$ absorbs light anisotropically, such that the π-bonded p orbitals of O and C atoms parallel to the crystal *c* axis exhibit maximum absorption when aligned parallel to linearly polarized light. The absorption intensity changes with a $\cos^2$ law with respect to the azimuthal orientation of the carbonate groups in the crystal. This information can reveal structural and mechanical properties in $CaCO_3$ biominerals (5). Coral biomineralization is a subject of intense studies, and the mechanisms of crystal nucleation and growth in coral skeletons are only beginning to be revealed (6–9).

The optical anisotropy in $CaCO_3$ has been leveraged in polarized visible light microscopy to study macroscopic biomineral structure and formation mechanisms (10, 11) and with imaging polarimetry to study crystal orientation uniformity (12, 13). In the shorter-wavelength regime, X-ray absorption near-edge structure spectroscopy has been used to study the orientations of various polymorphs of $CaCO_3$ (14, 15), and polarization-dependent imaging contrast (PIC) mapping using X-ray photoemission electron microscopy (X-PEEM) has been demonstrated to quantitatively map crystal orientations in $CaCO_3$ (15–17,). Currently, PIC mapping mostly uses X-PEEM in reflection geometry to achieve tens-of-nanometer resolution. However, PEEM's limited achievable spatial resolution (~20 nm) and the confinement to polished two-dimensional surfaces are insurmountable limits. Scanning transmission X-ray microscopy (STXM) has taken advantage of dichroic contrast to study polymer fibers (18) to resolve 30-nm features, but it is limited in achievable spatial resolution by the focusing optics, which also has a low efficiency and a short working-distance constraint.

Although macroscopic morphologies in biominerals have been studied extensively, their nanoscopic structures are still not studied routinely in a quantitative fashion, mostly due to the lack of a proper transmission microscope that offers bulk-sensitive information with spatial resolution down to the nanometer scale. With the development of high-brilliance synchrotron

Significance

Ptychography, a powerful scanning coherent diffractive imaging method, has attracted considerable attention for its general applicability. Here, we demonstrate X-ray linear dichroic ptychography to study the crystal orientations of the calcium carbonate in coral samples. In contrast to the absorption contrast commonly observed in linear dichroic imaging, dichroic ptychography at pre-oxygen K-edge shows significant and unique dichroic phase contrast, which has not been reported. The dichroic ptychography images reveal the presence of both narrow and wide *c*-axis angular spread in the submicrometer coral fragments, which are confirmed by 4D STEM. We expect X-ray linear dichroic ptychography to be a high-resolution, dose-efficient tool to broadly study optically anisotropic materials such as tooth enamel, bone, seashells, brittlestars, and polymers.

Author contributions: J.M. directed the project; P.U.P.A.G. and J.M. designed research; Y.H.L., J.Z., A.R., D.M., C.G., B.E., Y.-S.Y., C.-Y.S., D.A.S., R.W.F., H.C.K., M.M.M., P.U.P.A.G., and J.M. performed research; Y.H.L., J.Z., P.U.P.A.G., and J.M. analyzed data; and Y.H.L., P.U.P.A.G., and J.M. wrote the paper.

Competing interest statement: H.K. is partially employed by KMLabs, Inc.

This article is a PNAS Direct Submission.

[1]To whom correspondence may be addressed. Email: miao@physics.ucla.edu.

This article contains supporting information online at https://www.pnas.org/lookup/suppl/doi:10.1073/pnas.2019068118/-/DCSupplemental.

Published January 12, 2021.

radiation facilities worldwide, advancements in high-resolution imaging techniques, and the increasing availability of insertion-device X-ray sources providing polarization control, such as elliptically polarizing undulators (EPUs), new synchrotron-based tools are now becoming available for probing nanoscale crystal orientation in $CaCO_3$ minerals and biominerals. By taking advantage of brilliant X-ray sources, coherent diffractive imaging (CDI) can directly achieve high-resolution structural information of noncrystalline samples and nanocrystals from their diffraction patterns (19–28). In particular, ptychography, a scanning CDI technique (28), has attracted considerable attention for its general applicability (29–32). Ptychography measures a series of diffraction patterns from spatially overlapping illumination probes on a sample, where phase-retrieval algorithms are used to iteratively recover the incident wave and complex exit wave of the sample. This versatile diffractive imaging technique has been applied to study various biological materials in two and three dimensions with high resolution (33–40).

In this work, we present X-ray linear dichroic ptychography of biominerals using the aragonite ($CaCO_3$) coral skeleton of *Seriatopora aculeata* as a model. Aragonite is an orthorhombic $CaCO_3$ polymorph, with all three crystal axes being unequal in length and perpendicular to one another (1). Carbonate crystals grow acicularly with a needle-like habit and with 10 times greater growth rate along the *c* axis than along the *a* axis (41), resulting in densely packed bundles of thin crystals in coral skeletons. It has been hypothesized that this elongated growth pattern with crystals growing mostly along the fast *c* axis but in all directions is the most efficient way for aragonite fill 3D space (6). Consequently, this space-filling strategy may endow a unique evolutionary advantage to host organisms that adhere to the pattern by providing greater resilience to environmental stresses such as ocean acidification (42). Therefore, the exact nanoscopic mechanisms of biomineral growth along various crystal axes are of significant scientific interest in understanding the macroscopic structural changes in coral species around the world.

We imaged several coral-skeleton samples on and off the O K-edge π^* peak and observed significant contrast differences between absorption and phase images. Using three linear dichroic ptychography images, we performed PIC mapping to quantitatively determine crystal *c*-axis orientations in the coral with 35-nm spatial resolution. Our dichroic ptychography results were qualitatively validated by correlating the ptychography PIC maps with four-dimensional (4D) scanning transmission electron microscopy (STEM), a scanning nano-electron diffraction technique for probing crystal orientations in crystalline materials (43). We observed that, at the nanoscale, crystallite orientations can be narrowly distributed, as is characteristic of spherulitic crystals, but also randomly distributed in submicrometer particles. Moreover, we verified linear dichroic phase contrast at a pre-edge energy below the absorption resonance. The use of such phase contrast may lead to new dose-efficient dichroic imaging techniques for studying anisotropic biominerals and has important implications for understanding the nanoscale organization of crystallites in biominerals.

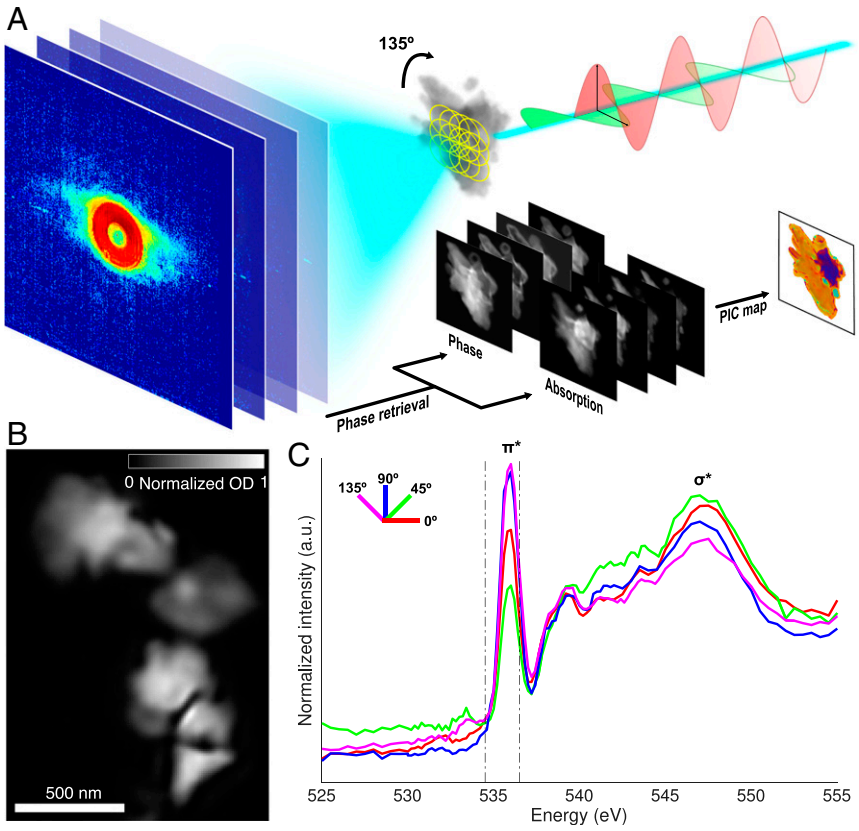

Fig. 1. Experimental schematic of X-ray linear dichroic ptychography. (*A*) Horizontally and vertically polarized X-rays incident on the specimen as spatially overlapping diffraction patterns were acquired below (534.5 eV) and on (536.5 eV) the O K-edge absorption edge to obtain 0° and 90° polarization data. The sample was then rotated 135° and measured again to obtain the 45° and 135° data. The diffraction patterns were directly phased to obtain high-resolution polarization-dependent ptychographic images, from which absorption images were used to compute the PIC maps. (*B*) Ptychography absorption image of a coral particle used to collect linear dichroic absorption spectra. (*C*) Experimental XAS spectra of the coral particle at four polarizations, showing the dependence of the $CaCO_3$ π^* peak intensity on the incident X-ray polarization angle. A.u., arbitrary units; OD, optical density.

Results

X-Ray Linear Dichroic Ptychography. Soft X-ray ptychographic microscopy measurements were performed at the imaging branch of the undulator beamline—COherent Scattering and MICroscopy (COSMIC)—at the Advanced Light Source (ALS) (44, 45). COSMIC provides monochromatic soft X-rays with energies variable from 250 to 2,500 eV, spanning the carbon and sulfur K-edges. Coherent and monochromatic X-rays were focused onto the sample by using a Fresnel zone plate, with 45-nm outer zone width and a total coherent flux of $\sim 10^9$ photons/s at the sample position. The transmission electron microscopy (TEM) grid containing the *S. aculeata* coral-skeleton sample was secured by using a Hummingbird 3-mm half-grid tip (*Materials and Methods*) and then mounted onto a standard FEI CompuStage sample manipulator derived from an FEI CM200 series TEM. Diffraction data were recorded with a 1,000-frame-store charge-coupled device (CCD) (46). Diffraction patterns were acquired without a beam stop and were automatically preprocessed onsite.

Ptychographic measurements consisted of single diffraction patterns recorded at each scan point with 200- or 300-ms dwell time and scanned in a square grid with 40-nm steps to cover a ~1.5- × 1.5-μm field of view, with a reconstruction pixel size of 10.1 nm/pixel. Linear dichroic ptychography data were collected at 0°, 45°, 90°, and 135° linear polarizations. The 0° and 90° data were collected with the EPU tuned to horizontal and vertical polarizations, respectively. Since, at the time of these measurements, only linear horizontal and vertical polarizations were under remote computer control, the TEM grid was physically rotated clockwise in-plane by ~135° with respect to the upstream beam, and then the 45° and 135° data were collected by using the horizontal and vertical polarizations again.

The same linear dichroic data with four polarization angles were collected at two X-ray energies around the O K-edge π* peak: one pre-edge (at 534.5 eV, or 1.5 eV before the π* peak) and another on-peak (at 536.5 eV, or 0.5 eV after the π* peak maximum). The pre-edge energy was estimated to be near the negative phase peak and, thus, had the most negative phase shift relative to vacuum to achieve optimal phase contrast. The on-peak energy was chosen to be slightly off the maximum absorption peak at 536 eV to reduce beam absorption and attenuation caused by specimen thickness. The resonant energy at the O edge rather than the C edge was chosen in this study because the 3:1 ratio of O to C in $CaCO_3$ means imaging at O resonance gives three times higher signal-to-noise ratio and contrast. After all data were acquired, ptychography reconstructions were performed by using a regularized ptychographic iterative engine (47) with 300 iterations, with $\beta_{obj} = 0.7$ and $\beta_{probe} = 0.7$, and updating the initial probe only after the 100th iteration.

Fig. 1 shows the experimental schematic of the linear dichroic X-ray ptychography experiment. Fig. 1*C* shows the O K-edge spectra obtained from STXM with X-ray absorption spectroscopy (XAS) at each linear polarization (*Materials and Methods*), showing the expected dependence of X-ray absorption on the relative angle between crystal *c*-axis and X-ray polarization (15). The π* peak absorption occurs around 536 eV and is maximum when X-ray polarization is parallel to the π orbitals of C and O in the trigonal planar carbonate group. The broad σ* peak occurs around 547 eV and is anticorrelated with the π* peak.

To study the effects of linear dichroism on the absorptive component of the coral's complex exit wave, we imaged three coral particles at two energies, pre- and on-peak. Fig. 2*A* shows on-peak ptychography absorption contrast images of three coral particles at 0°, 45°, 90°, and 135° polarizations from top to bottom, and the particles are denoted from left to right as P1, P2, and P3, respectively. Relative contrast within the particles changes dramatically with polarization, signifying the presence of differently oriented nanoscale domains in each particle. P1 displayed overall smooth features with little internal structures, whereas P2 and P3 contained multiple nanodomains and striations. While resonant imaging revealed rich polarization-dependent absorption contrast due to the linear dichroism, imaging off resonance produced no absorption contrast when varying polarizations (*SI Appendix*, Fig. S3*A*).

To examine the effects of linear dichroism on the phase component of the complex exit wave of the coral-skeleton particles, we also measured ptychographic images at 534.5 eV (Fig. 2*B*), an energy slightly before the π* peak. In general, the negative phase peak is at lower energy than both the positive phase peak and the absorption peak and provides the greatest contrast with respect to nonresonant material (48). Phase-contrast images revealed sharp boundaries and complex surface morphologies in the particles. On the other hand, on-edge phase images of the coral particles revealed polarization-dependent contrast that agreed very well with on-edge absorption images (*SI Appendix*, Fig. S3*B*). According to the Kramers–Kronig relation, the effects of linear dichroism in crystal orientation manifest in both components of the complex refractive index. But as we observed in ptychographic maps, while the effect on absorption was significant on resonance (Fig. 2*A*), the effect on phase was maximum off resonance (Fig. 2*B*). Resolution of the ptychographic images was estimated to be 35 nm by using the knife-edge method with 10 to 90% intensity cutoff (*SI Appendix*, Fig. S4). Given a mass attenuation coefficient (μ/ρ) of 2×10^4 cm^2/g for $CaCO_3$ on O K-edge and an ~50% overlap, each recorded projection absorbed an estimated dose of 1.44×10^8 Gy. At this dose and estimated resolution, no noticeable deterioration was observed in the sample (49).

PIC Mapping. Ptychographic PIC mapping revealed that the orientations of crystals were much more diverse at the nanoscale than previously appreciated (*Materials and Methods*). As is clear from Fig. 3, and, in particular, from the broad range of colors in the three particles in Fig. 3*A* and the large width of the histograms in Fig. 3*B*, many crystallites were present in what was previously assumed to be single crystals (e.g., P2) or two crystals (e.g., P1). These crystallites varied in orientation gradually, as displayed by color gradients across all larger domains, as in the mustard-color domain of P1, the green-blue domain of P2, or the yellow-red-blue domain of P3. There were also unexpected, smaller (~100 nm) domains with orientation different from the larger domain, but not randomly oriented as expected from sample preparation artifacts, e.g., randomly aggregated particles. These small domains were co-oriented with one another, but spatially separate from one another. Other smaller domains in P2 were the red-dot crystallites near the edges. P3 shows several blue-green crystals of similar smaller sizes and orientations, that are interspersed with the rest of the particle shown as yellow-red-yellow. These nano-crystallites are highly surprising, as they were not revealed by previous methods, such as PIC mapping using X-PEEM in previous work (6, 9) or in this work in *SI Appendix*, Fig. S5 (*Materials and Methods*). PEEM-PIC mapping shows that the smaller crystalline domains in the centers of calcification are randomly oriented in *Seriatopora aculeata* coral skeletons (*SI Appendix*, Fig. S5). Ptychographic PIC mapping, instead, shows that several smaller (~100 nm) crystallites are misoriented with respect to the larger crystal domains in which they are embedded, but co-oriented with one another (Fig. 3*A*).

To better understand the co-oriented smaller domains, we performed PIC mapping on the on-edge linear dichroic ptychography absorption images to quantitatively map *c*-axis angles in the coral particles and analyzed the in-plane (γ) and out-of-plane (χ) *c*-axis orientation angles (*Materials and Methods*). The PIC maps in Fig. 3*A* were calculated by using the 0°, 45°, and 90° polarization images, and a second set of PIC maps was computed by using 0°, 135°, and 90° polarization images (*SI Appendix*, Fig. S6). In

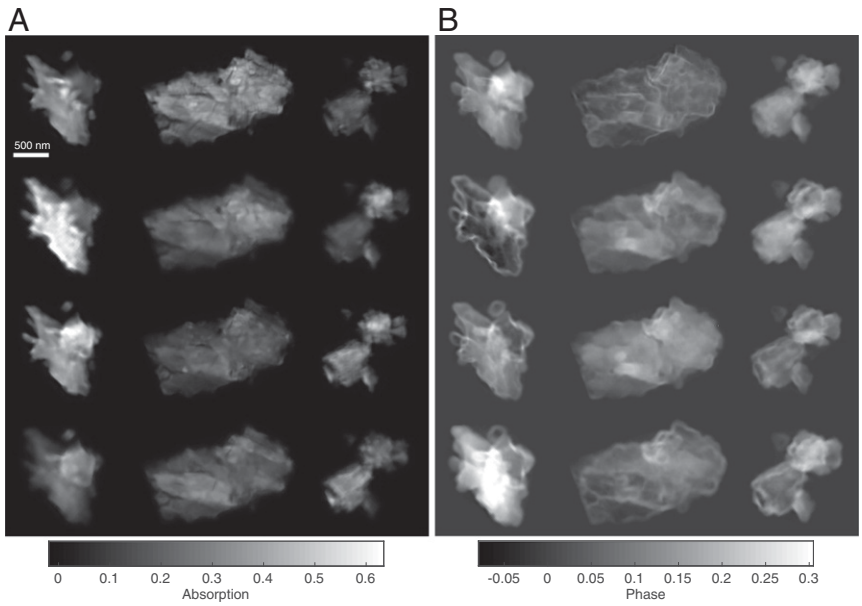

Fig. 2. X-ray linear dichroic ptychography of coral-skeleton particles. (*A*) Ptychography absorption images of three aragonite particles (P1, P2, and P3, from left to right) recorded on the O K-edge absorption resonance at 536.5 eV (Fig. 1*C*), across four linear polarizations (top to bottom: 0°, 45°, 90°, and 135°), showing strong polarization-dependent absorption contrast and revealing nanoscale morphologies ranging from smooth homogeneous particles several hundred nanometers in size to sub-100-nm fine features. (*B*) Ptychography phase images of the same particles and polarizations recorded at an energy slightly before O K-edge absorption edge of 534.5 eV (Fig. 1*C*), showing strong polarization-dependent phase contrast and more edge-sensitive features in internal coral structures.

each PIC map, in-plane angles are color-coded according to the coral's crystal axes relative to the X-ray polarization, which is horizontal at 0°. Orientation ranges from 0° to 90°, since angles beyond that range are degenerate and cannot be distinguished from contrast alone. The out-of-plane angles between the *c*-axes and X-ray polarization are represented by brightness, such that *c*-axes aligned with the imaging plane are displayed with high brightness, and *c*-axes that are perpendicular to the imaging plane are shown in low brightness, and are lowest when the axes align directly with the X-ray beam.

Histograms of γ (*Upper*) and χ (*Lower*) in Fig. 3*B* present the *c*-axis angular distribution derived from the PIC maps. P1 exhibits two distinct subdomains, within which the angular spread is <35°, but these are oriented more than 35° apart from one another. In contrast, P2 and P3 show greater submicrometer orientational fluctuations that span more than 35°, suggesting that particles P2 and P3 comprise many differently oriented nanocrystals from the centers of calcification. To examine the abrupt orientational change between subdomains in P1, we performed electron tomography on the same P1 particle (*Materials and Methods*), which revealed two separate particles on top of each other and, thus, confirmed the ptychography results (*SI Appendix*, Fig. S7).

The 4D STEM and Clustering Analysis. To validate the localization and orientation of crystallites observed in ptychographic PIC maps, we performed a 4D STEM experiment on particle P3 and assessed its nanoscale lattice changes over the entire particle (*Materials and Methods*). The converging beam electron diffraction (CBED) patterns were analyzed by using unsupervised agglomerative hierarchical clustering to sort the particle into different regions with similar crystal orientations (50). Fig. 4 *A* and *B* show a STEM image of P3 and the resulting similarity ranking map generated by hierarchical clustering, respectively. The closer the regions are in color, the more similar their corresponding CBED patterns are. Representative CBED patterns from the coral skeleton are shown in Fig. 4*C*, with numbers corresponding to the labeled regions in Fig. 4*B*.

The CBED patterns reveal variations and similarity in diffraction—hence, crystal orientations—across the particle. For instance, pattern 1 is similar to pattern 9, and both are in close proximity to one another. In contrast, patterns 4 and 6, although within the same region, have dissimilar diffraction patterns. Moreover, the similarity ranking map divides the particle P3 into subregions closely resembling those shown in the ptychographic PIC map in Fig. 3*A*. In particular, distinct subdomains in regions 2, 3, 4, and 7 of the similarity ranking map match well with the corresponding areas in the ptychographic PIC map. This result serves as further confirmation of the orientation heterogeneity within P3.

Discussion

X-ray linear dichroic ptychography of coral particles shown in Fig. 2 unveils strong polarization-dependent absorption and phase contrast that are evidence of differently oriented subdomains in each particle. Moreover, each particle exhibits diverse structural features and contains crystal-orientation domains that range in size from tens to hundreds of nanometers. While both on-edge absorption and pre-edge phase images reveal fine internal features in the coral-skeleton particles, phase images are more sensitive to edges and, thus, show surface morphologies and boundaries more clearly. The use of phase information to visualize weakly scattering fine features has previously been demonstrated with visible light-phase ptychography to enhance cellular contrast in live cells (51). In the case of biominerals, the simultaneous phase and absorption contrast imaging provided by X-ray ptychography can be used to probe nanoscale boundary features beyond the surface, enabling structural study of intercrystal topology that is critical in understanding biomineral nucleation and growth. This is a demonstration of combined linear dichroic absorption and phase imaging of optically anisotropic materials.

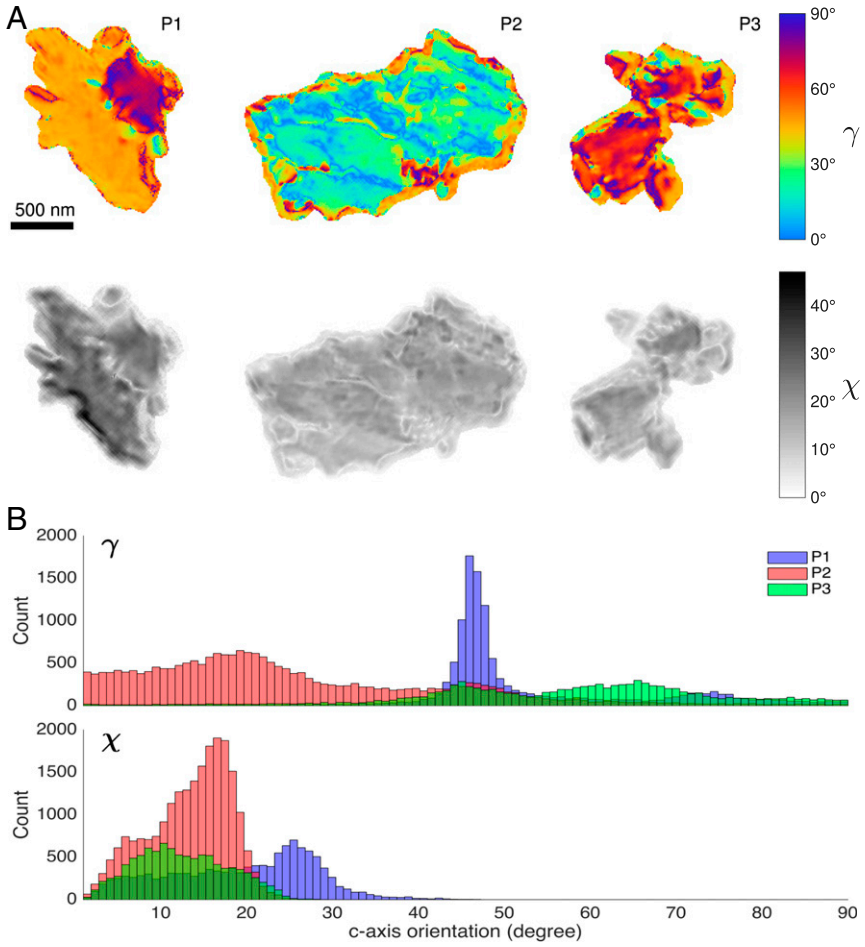

Fig. 3. Ptychography PIC map of aragonite coral-skeleton particles. (*A*) Quantitative PIC maps of the three aragonite particles, calculated using 0°, 45°, and 90° linear dichroic ptychography images. Hue (*Upper*) denotes in-plane azimuthal crystal *c*-axis angle (γ) of the crystallite, while brightness (*Lower*) denotes out-of-plane *c*-axis angle (χ), all ranging from 0° to 90°. P1 consists of mostly homogeneous orientations, whereas P2 and P3 show more orientational diversity. (*B*) Histograms of in-plane (γ; *Upper*) and out-of-plane (χ; *Lower*) angles for the three particles, showing a narrow γ angular spread (<35°) for P1 and broader spread (>35°) for P2 and P3, suggesting the presence of both spherulitic and randomly oriented submicrometer crystallites at the nanoscopic scale.

The orientations observed in the main domains of each particle are <35°, as previously observed (6, 42, 52), and are consistent with spherulitic crystals (6). PIC maps generated from the X-ray linear dichroic ptychography images (Fig. 2 and *SI Appendix*, Fig. S3) provide quantitative crystal-orientation information with high resolution and at a depth on the order of 100 to 500 nm, which is not available with the 5-nm-surface-sensitive X-PEEM PIC mapping (*SI Appendix*, Fig. S5). At the fine-grain level, the ptychographic PIC map of P1 shows the presence of two overlaid homogeneous particles, each having a *c*-axis angular spread of <35° (Fig. 3*B*). Such narrow angular spread is typical of spherulitic crystal such as those that form all coral skeletons, fills space isotropically with anisotropic crystals, and thus provides the coral skeleton with the needed structural support (6, 9).

Similarly, the main crystalline domains in all three particles, P1, P2, and P3, are co-oriented within 35°, as expected from spherulitic crystals. But, surprisingly, all three particles exhibit several smaller (~100 nm) domains differently oriented with respect to the main domain (Fig. 3). Since the orientations of these smaller domains are not random, but co-oriented with one another, these crystallites cannot be the randomly oriented nanocrystals termed sprinkles observed at growth fronts in some coral species (9) or in CoC in others such as *Acropora* sp. (9), including *Seriatopora aculeata* studied here (*SI Appendix*, Fig. S5). These smaller co-oriented domains in corals have not been observed with such detail before, presumably because previous studies did not have the capability to detect bulk subdomain morphology. Evidence of such co-oriented, disconnected corallites cannot be easily explained by current models for coral-skeleton formation (7, 53, 54). Although additional evidence is needed to fully understand the source and formation mechanism of the observed co-oriented, disconnected crystallites, any model for coral-skeleton growth must be consistent with their formation.

The X-ray linear dichroic ptychography results presented in this work imply an important possibility. Conventionally, enhanced polarization-dependent contrast is derived from absorption contrast when imaged on elemental absorption edges, with the trade-off being that more energy is deposited into the sample per unit area and time, which inevitably exacerbates sample radiation damage. However, as this work has demonstrated, one major benefit of X-ray linear dichroic ptychography is that strong polarization-dependent phase contrast is also available when imaged at the off-resonant energy. Benefits of off-resonance, dose-efficient imaging have been reported (48, 55), in which the large phase shifts and strong energy dependence near atomic resonances play an important role in achieving high spatial resolution. It was observed that the maximum resolution peak falls at the energy of the most negative phase shift relative to vacuum, which yields the maximum phase

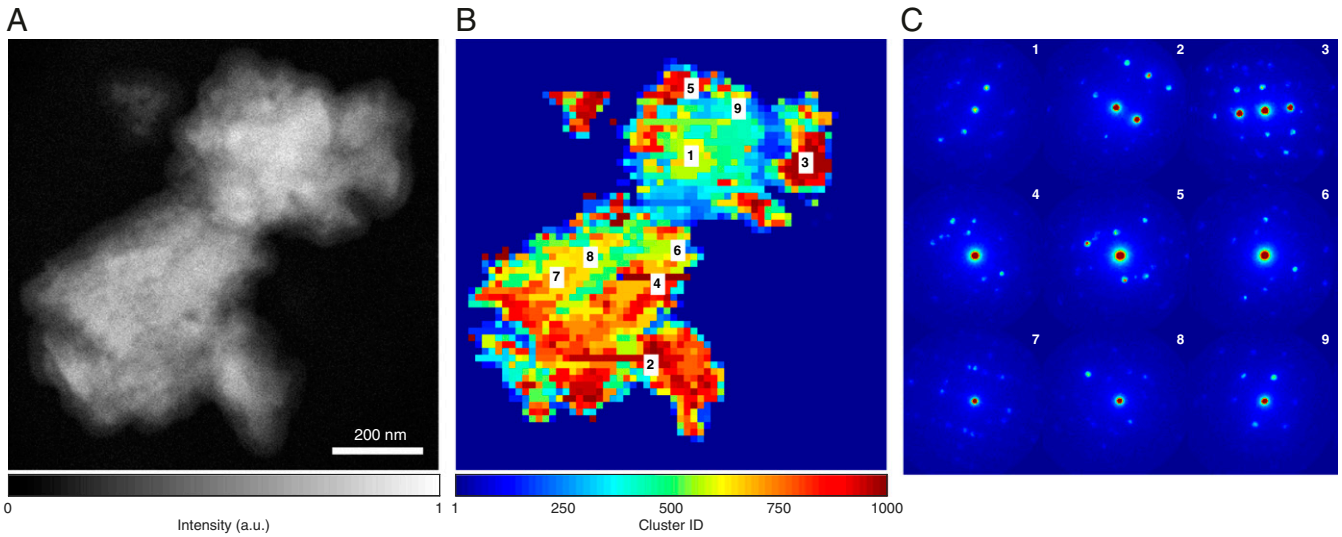

Fig. 4. Diffraction similarity map from 4D STEM with hierarchical clustering. (*A*) STEM image of particle P3, which was used to acquire scanning electron nano-diffraction patterns. (*B*) Crystal axis similarity map generated using hierarchical clustering of diffraction patterns. Areas with comparable color resemble subdomains with similar crystal orientations. The resulting map qualitatively agrees with the PIC map generated from ptychography PIC mapping (P3 in Fig. 3). (*C*) Representative CBED patterns from various regions of the coral particle, colabeled in *B* and *C*, showing nanoscale orientational diversity. (Scale bar, 200 nm.) A.u., arbitrary units.

contrast relative to the nonresonant material and points to phase contrast being a primary driver in ptychographic image resolution.

Altogether, our study indicates that linear dichroic phase-contrast imaging offers an alternative path to obtaining quantitative crystal-orientation insights without having to subject the sample to the same radiation dose as absorption-edge imaging. This potentially important finding can enable more sophisticated and data-intensive studies. Such dose-efficient technique will be especially advantageous when applying vector ptychographic tomography to biomaterials (56, 57), since many tilt projections are needed to achieve high-quality 3D reconstruction. So far, most linear dichroism studies focused on absorption, because linear phase dichroism was difficult to obtain experimentally. Thus, X-ray linear dichroic phase ptychography has the potential to become an important tool for studying dose-sensitive materials.

Conclusion

In this work, we present an experimental demonstration of X-ray linear dichroic ptychography. By imaging three *S. aculeata* coral-skeleton particles at pre- and on-peak O K-edge energies, we observed strong polarization-dependent phase and absorption contrasts. We performed PIC mapping on the dichroic ptychography absorption images to quantitatively estimate *c*-axis orientations in the corals and observed the presence of two types of previously known crystallites: a main domain in each particle with narrow angular spread $< 35°$ consistent with spherulitic crystals and with the randomly oriented submicrometer nanocrystal domains observed in the centers of calcification of *Acropora* coral skeletons (9). Furthermore, we observed ∼100-nm crystallites misoriented with respect to the main domains in each particle, but co-oriented with one another, disconnected, and interspersed with and within larger crystals. We validated the X-ray dichroic ptychography results with 4D STEM and confirmed that regions of orientational diversity are largely consistent. The observation of strong linear phase dichroism off the absorption edge offers the potentially interesting possibility of using phase imaging rather than absorption imaging in future linear dichroism studies as a way to alleviate sample radiation damage. Although we used coral samples as a proof-of-principle in this work, we anticipate that X-ray linear dichroic ptychography can be coupled with 4D STEM and spatially resolved X-ray scattering (58) to study a wide range of optically anisotropic materials such as tooth enamel (59), bone (60), seashells (61), brittlestars (62), and polymers (18) at multiple length scales.

Materials and Methods

***S. aculeata* Skeleton Preparation.** The *S. aculeata* coral skeleton used in this study was a pencil-thick, short, and tapered branch, termed a nubbin (*SI Appendix*, Fig. S1). An entire *S. aculeata* coral skeleton, $\sim 10 \times 10 \times 10$ cm^3 in size, was purchased from Tropical Fish World. To remove the tissue and obtain a clean aragonite skeleton, the living coral was immersed in 5% sodium hypochloride in water (Chlorox). After 7 d of bleaching, the skeleton was washed twice in double-distilled H_2O for 5 min and twice in ethanol for 5 min. An ∼1-cm-long nubbin was broken off from the rest of the coral skeleton, placed in an agate mortar, and immersed in 100% ethanol, then gently fractured by an agate pestle into micrometer-sized grains. The resulting ethanol suspension was sonicated for 2 min for further dispersion, and the supernatant solution was transferred by pipette onto a 200 mesh copper TEM grid coated with carbon film and air-dried for 24 h before data acquisition.

XAS. STXM-XAS was measured at ALS beamline 7.0.1.2. The spectromicroscopy data were recorded with 5-ms dwell time and proceeded with 60-nm steps in a square grid scan, with energies spanning the entire O K-edge from 525 to 555 eV. Energy-scan steps proceeded with 0.5-eV steps from 525 to 530 eV, then 0.2 eV from 530 to 542 eV, and, finally, with 0.5-eV steps from 542 to 555 eV. The same energy-scan parameters were repeated for X-ray linear polarizations at 0°, 45°, 90°, and 135°. All spectra were normalized via subtraction of the average image from nonresonant energies from 525 to 530 eV.

X-ray absorption spectra were generated by using the MANTiS software (63). STXM-XAS images at each linear polarization were first converted to optical densities by using fully transmitting regions in the specimen, then aligned by using cross-correlation. Principal component analysis was used to reduce the dimensionality of spectral information in the images to obtain absorption signatures of the coral. The first principal component spectrum at each polarization, which represents the average absorption present in the coral, is shown in *SI Appendix*, Fig. S2.

Ptychographic PIC Mapping. Crystallographic *c*-axis orientations in coral particles were calculated by using PIC mapping (16), a method that uses linear dichroism effects to quantitatively determine the angular orientation of microcrystals and nanocrystals. We used the closed-form expression to compute the in-plane angle, χ, and out-of-plane angle, γ, of the crystal *c* axis

with respect to the linear polarization vector. Here, in-plane is defined as the TEM grid plane that is perpendicular to the X-ray beam. Given three EPU polarization angles, 0°, 90°, and 45°, the electric field vectors at each polarization were $\vec{E}_1 = E_0\hat{x}$, $\vec{E}_2 = E_0\hat{y}$, and $\vec{E}_3 = (\vec{E}_1 + \vec{E}_2)/\sqrt{2}$, where $\hat{x}$ and $\hat{y}$ are unit vectors. The unit vector describing the *c*-axis orientation is $\hat{c} = \hat{x}\sin\chi\cos\gamma + \hat{y}\sin\chi\sin\gamma + \hat{z}\cos\chi$. For the *i*th polarization, the signal intensity was $I_i = I_A + I_B(\vec{E}_i \cdot \vec{c})$, where I_A and I_B are positive fitting parameters. Algebraic manipulations of the three components yield

$$\cos^2\gamma = \frac{1}{2} + \frac{I_1 - I_2}{2\left[(I_1 - I_2)^2 + (I_1 + I_2 - 2I_3)^2\right]^{1/2}}, \quad [1]$$

$$\sin^2\chi = \frac{1}{I_B}\left[(I_1 - I_2)^2 + (I_1 + I_2 - 2I_3)^2\right]^{1/2}. \quad [2]$$

Solving for γ and χ in the above equations gives the in-plane and out-of-plane *c*-axis angles, respectively. The range of χ contracts and expands as I_B varies, but the relative difference in χ between particles remains consistent. In this work, I_B was arbitrarily set to two. Since ptychography data at four EPU linear polarizations were collected, two sets of polarizations were used to calculate two PIC maps for each coral particle: the first set used 0°, 45°, and 90°, and the second set used 0°, 135°, and 90°.

PEEM-PIC Mapping. The PIC maps were acquired by using the PEEM-3 instrument on Beamline 11.0.1.1 at ALS. Nine partly overlapping 60-μm × 60-μm PIC map data were acquired and then tiled and blended in Photoshop. For each PIC map, a stack of 19 PEEM images was acquired on-peak at the O K-edge π* energy as the linear polarization from the undulator was rotated from 0° to 90° in 5° increments. The 19 images were mounted as a stack and analyzed for fully quantitative crystal-orientation information in each 60-nm pixel by using the GG Macros in Igor Pro Carbon. As coral skeletons are made of <99.9% aragonite ($CaCO_3$) and <0.1% organic matrix (64), the contribution of organics to oxygen spectroscopy is <<0.1%, which is not expected to exhibit any polarization dependence. Thus, PIC mapping in ptychography or PEEM only displays aragonite crystal orientations.

The 4D STEM and Electron Tomography. The 4D STEM and electron tomography data were collected at the National Center for Electron Microscopy, Molecular Foundry, Lawrence Berkeley National Laboratory. Both methods were used on the same three samples already analyzed with ptychography. A Titan 60-300 equipped with an Orius 830 detector (Gatan) and four windowless silicon drift energy-dispersive detectors (FEI super-X) were used with a solid angle of 0.7 srad. The microscope operated in STEM mode at 200 kV with an electron-beam current of ∼16 pA for 4D STEM datasets and ∼40 pA for STEM imaging. The 4D STEM diffraction patterns were taken on an Orius CCD with a camera length of 300 mm using a convergence angle ∼0.51 mrad, with 64 × 64 square grid scan positions. Before clustering of 4D STEM data, individual diffraction patterns were preprocessed by aligning the center of mass of the main beam to the image center to correct for horizontal and vertical shifts introduced by beam tilt.

A diffraction-similarity map was generated by using agglomerative hierarchical clustering (50) of 4D STEM data. Agglomerative hierarchical clustering initialized all data points, or individual diffraction patterns, as independent clusters. The algorithm then computed the proximity between every pair of data points using a specified distance metric (e.g., Euclidean distance, cosine similarity, or correlation). Next, pairs of data points were linked to one another by using a specified linkage metric (e.g., average distance, centroid distance, or nearest-neighbor distance) to form new grouped clusters and repeated until all data points were linked together into a hierarchical tree. Finally, the consistency of the resulting clusters was verified by evaluating the distances between each pair of neighboring clusters in the tree. A distance that was greater than a predefined inconsistency score constituted a natural partition between clusters, such that separate clusters were considered to be truly independent. This clustering was performed in a MATLAB (MathWorks) environment with the "linkage" function, using correlation as the distance metric, nearest neighbor as the linkage metric, and an inconsistency score of 1.2.

Electron tomography was performed by using the GENeralized Fourier Iterative REconstruction (GENFIRE) (65), an algorithm that has been used to determine the 3D and 4D atomic structure in materials with unprecedented detail (66–68). Before reconstruction, STEM projections were aligned to a common tilt axis by using the center-of-mass and common-line methods (69). Next, a constant background—the average value in an empty region of the image—was subtracted from each projection, and the process was optimized by minimizing the differences between all common lines and a reference common line. The projections were then normalized to have the same total sum, since the integrated 3D density of the isolated coral particle should be consistent across all tilt angles. The preprocessed projections were used in GENFIRE reconstruction, which ran for 100 iterations with an oversampling ratio of two (70), 0.7-pixel interpolation distance, and the enforcement of positivity and support constraints.

Data Availability. X-ray linear dichroic ptychography data presented in this work are available for download at the Coherent X-Ray Imaging Data Bank (https://www.cxidb.org/id-109.html), and electron tomography data presented in this work are available for download at Mendeley Data (https://data.mendeley.com/datasets/f62bfbndym/1). All data needed to evaluate the conclusions in the paper are present in the paper and/or *SI Appendix*.

ACKNOWLEDGMENTS. We thank Marcus Gallagher-Jones for guidance on 4D STEM analysis and Jared J. Lodico and Billy A. Hubbard for help handling the samples during the ptychography experiments at COSMIC. We thank NVIDIA Corporation for the donation of the Quadro K5200 GPU used for this research. This work was primarily supported by STROBE: A NSF Science & Technology Center under Grant DMR 1548924. The 4D STEM and electron tomography work were supported by the Department of Energy (DOE), Office of Science, Basic Energy Sciences (BES), Division of Materials Sciences and Engineering Award DE-SC0010378. P.U.P.A.G. received 40% support from DOE–BES–Chemical Sciences, Geosciences, Biosciences–Geosciences Grant DE-FG02-07ER15899, 40% support from the Laboratory Directed Research and Development (LDRD) program at Berkeley Lab, through DOE-BES, under Award Number DE-AC02-05CH11231, and 20% support from NSF Biomaterials Grant DMR-1603192. All X-ray experiments were done at the ALS, which is supported by the Director, Office of Science, BES, DOE Contract DE-AC02-05CH11231. The 4D STEM and electron tomography experiments were performed at the Molecular Foundry, which is supported by Office of Science, BES, DOE Contract DE-AC02-05CH11231. The electron tomography data were based on high-angle annular dark-field STEM images. D.M. was supported by the DOE National Nuclear Security Administration Stewardship Science Graduate Fellowship program, which is provided under Grant DENA0003864.

1. H. A. Lowenstam, S. Weiner, *On Biomineralization* (Oxford University Press, Oxford, UK, 1989).
2. U. G. K. Wegst, H. Bai, E. Saiz, A. P. Tomsia, R. O. Ritchie, Bioinspired structural materials. *Nat. Mater.* **14**, 23–36 (2015).
3. Z. Yin, F. Hannard, F. Barthelat, Impact-resistant nacre-like transparent materials. *Science* **364**, 1260–1263 (2019).
4. N. K. Dhami, M. S. Reddy, A. Mukherjee, Biomineralization of calcium carbonates and their engineered applications: A review. *Front. Microbiol.* **4**, 314 (2013).
5. J. Stöhr, K. Baberschke, R. Jaeger, R. Treichler, S. Brennan, Orientation of chemisorbed molecules from surface-absorption fine-structure measurements: CO and NO on Ni(100). *Phys. Rev. Lett.* **47**, 381–384 (1981).
6. C.-Y. Sun *et al*., Spherulitic growth of coral skeletons and synthetic aragonite: Nature's three-dimensional printing. *ACS Nano* **11**, 6612–6622 (2017).
7. T. Mass *et al*., Amorphous calcium carbonate particles form coral skeletons. *Proc. Natl. Acad. Sci. U.S.A.* **114**, E7670–E7678 (2017).
8. Chang-Yu Sun *et al*., From particle attachment to space-filling coral skeletons. *Proc. Natl. Acad. Sci. U.S.A.* **117** (48), 30159–30170 (2020).
9. Chang-Yu Sun *et al*., Crystal nucleation and growth of spherulites demonstrated by coral skeletons and phase-field simulations. *Acta Biomater.*, 10.1016/j.actbio.2020.06.027 (2020).
10. M. J. Olszta, D. J. Odom, E. P. Douglas, L. B. Gower, A new paradigm for biomineral formation: Mineralization via an amorphous liquid-phase precursor. *Connect. Tissue Res.* **44**, 326–334 (2003).
11. I. M. Weiss, N. Tuross, L. Addadi, S. Weiner, Mollusc larval shell formation: Amorphous calcium carbonate is a precursor phase for aragonite. *J. Exp. Zool.* **293**, 478–491 (2002).
12. R. A. Metzler, J. A. Jones, A. J. D'Addario, E. J. Galvez, Polarimetry of *Pinctada fucata* nacre indicates myostracal layer interrupts nacre structure. *R. Soc. Open Sci.* **4**, 160893 (2017).
13. R. A. Metzler, C. Burgess, B. Regan, S. Spano, E. J. Galvez, "Polarimetry of nacre in iridescent shells," in *The Nature of Light: Light in Nature V*, R. Liang, J. A. Shaw, Eds. (Proceedings of SPIE, International Society for Optics and Photonics, Bellingham, WA, 2014), vol. 9187, p. 918704.
14. R. A. Metzler *et al*., Architecture of columnar nacre, and implications for its formation mechanism. *Phys. Rev. Lett.* **98**, 268102 (2007).
15. R. T. DeVol *et al*., Oxygen spectroscopy and polarization-dependent imaging contrast (PIC)-mapping of calcium carbonate minerals and biominerals. *J. Phys. Chem. B* **118**, 8449–8457 (2014).
16. P. U. P. A. Gilbert, A. Young, S. N. Coppersmith, Measurement of c-axis angular orientation in calcite ($CaCO_3$) nanocrystals using X-ray absorption spectroscopy. *Proc. Natl. Acad. Sci. U.S.A.* **108**, 11350–11355 (2011).

17. Pupa U.P.A Gilbert *et al*., Nacre tablet thickness records formation temperature in modern and fossil shells. *Earth Planet. Sci. Lett.* **460**, 281–292 (2017).
18. H. Ade, B. Hsiao, X-ray linear dichroism microscopy. *Science* **262**, 1427–1429 (1993).
19. J. Miao, P. Charalambous, J. Kirz, D. Sayre, Extending the methodology of X-ray crystallography to allow imaging of micrometre-sized non-crystalline specimens. *Nature* **400**, 342–344 (1999).
20. J. Miao *et al*., Imaging whole *Escherichia coli* bacteria by using single-particle X-ray diffraction. *Proc. Natl. Acad. Sci. U.S.A.* **100**, 110–112 (2003).
21. H. N. Chapman *et al*., High-resolution ab initio three-dimensional x-ray diffraction microscopy. *J. Opt. Soc. Am. A Opt. Image Sci. Vis.* **23**, 1179–1200 (2006).
22. C. Song *et al*., Quantitative imaging of single, unstained viruses with coherent x rays. *Phys. Rev. Lett.* **101**, 158101 (2008).
23. H. Jiang *et al*., Nanoscale imaging of mineral crystals inside biological composite materials using X-ray diffraction microscopy. *Phys. Rev. Lett.* **100**, 038103 (2008).
24. I. Robinson, R. Harder, Coherent X-ray diffraction imaging of strain at the nanoscale. *Nat. Mater.* **8**, 291–298 (2009).
25. Y. Nishino, Y. Takahashi, N. Imamoto, T. Ishikawa, K. Maeshima, Three-dimensional visualization of a human chromosome using coherent X-ray diffraction. *Phys. Rev. Lett.* **102**, 018101 (2009).
26. M. M. Seibert *et al*., Single mimivirus particles intercepted and imaged with an X-ray laser. *Nature* **470**, 78–81 (2011).
27. J. A. Rodriguez *et al*., Three-dimensional coherent X-ray diffractive imaging of whole frozen-hydrated cells. *IUCrJ* **2**, 575–583 (2015).
28. J. Miao, T. Ishikawa, I. K. Robinson, M. M. Murnane, Beyond crystallography: Diffractive imaging using coherent x-ray light sources. *Science* **348**, 530–535 (2015).
29. J. M. Rodenburg, H. M. Faulkner, A phase retrieval algorithm for shifting illumination. *Appl. Phys. Lett.* **85**, 4795–4797 (2004).
30. P. Thibault *et al*., High-resolution scanning x-ray diffraction microscopy. *Science* **321**, 379–382 (2008).
31. D. A. Shapiro *et al*., Chemical composition mapping with nanometre resolution by soft X-ray microscopy. *Nat. Photonics* **8**, 765–769 (2014).
32. F. Pfeiffer, X-ray ptychography. *Nat. Photonics* **12**, 9–17 (2018).
33. K. Giewekemeyer *et al*., Quantitative biological imaging by ptychographic x-ray diffraction microscopy. *Proc. Natl. Acad. Sci. U.S.A.* **107**, 529–534 (2010).
34. M. Dierolf *et al*., Ptychographic X-ray computed tomography at the nanoscale. *Nature* **467**, 436–439 (2010).
35. J. Deng *et al*., Simultaneous cryo X-ray ptychographic and fluorescence microscopy of green algae. *Proc. Natl. Acad. Sci. U.S.A.* **112**, 2314–2319 (2015).
36. I. Zanette *et al*., Ptychographic X-ray nanotomography quantifies mineral distributions in human dentine. *Sci. Rep.* **5**, 9210 (2015).
37. M. E. Birkbak, M. Guizar-Sicairos, M. Holler, H. Birkedal, Internal structure of sponge glass fiber revealed by ptychographic nanotomography. *J. Struct. Biol.* **194**, 124–128 (2016).
38. M. Gallagher-Jones *et al*., Correlative cellular ptychography with functionalized nanoparticles at the Fe L-edge. *Sci. Rep.* **7**, 4757 (2017).
39. F. Mastropietro *et al*., Revealing crystalline domains in a mollusc shell single-crystalline prism. *Nat. Mater.* **16**, 946–952 (2017).
40. J. Deng *et al*., Correlative 3D x-ray fluorescence and ptychographic tomography of frozen-hydrated green algae. *Sci. Adv.* **4**, eaau4548 (2018).
41. A. Lin, M. A. Meyers, Growth and structure in abalone shell. *Mater. Sci. Eng. A* **390**, 27–41 (2005).
42. I. Coronado, M. Fine, F. R. Bosellini, J. Stolarski, Impact of ocean acidification on crystallographic vital effect of the coral skeleton. *Nat. Commun.* **10**, 2896 (2019).
43. C. Ophus, Four-dimensional scanning transmission electron microscopy (4D-STEM): From scanning nanodiffraction to ptychography and beyond. *Microsc. Microanal.* **25**, 563–582 (2019).
44. R. Celestre *et al*., Nanosurveyor 2: A compact instrument for nano-tomography at the Advanced Light Source. *J. Phys. Conf. Ser.* **849**, 012047 (2017).
45. D. A. Shapiro *et al*., Ptychographic imaging of nano-materials at the Advanced Light Source with the nanosurveyor instrument. *J. Phys. Conf. Ser.* **849**, 012028 (2017).
46. D. Doering *et al*., "High speed, direct detection 1k Frame-Store CCD sensor for synchrotron radiation" in *2011 IEEE Nuclear Science Symposium Conference Record* (IEEE, Piscataway, NJ, 2011), pp. 1840–1845.
47. A. Maiden, D. Johnson, P. Li, Further improvements to the ptychographical iterative engine. *Optica* **4**, 736–745 (2017).
48. M. Farmand *et al*., Near-edge X-ray refraction fine structure microscopy. *Appl. Phys. Lett.* **110**, 063101 (2017).
49. M. R. Howells *et al*., An assessment of the resolution limitation due to radiation-damage in x-ray diffraction microscopy. *J. Electron Spectrosc. Relat. Phenom.* **170**, 4–12 (2009).
50. L. Rokach, O. Maimon, "Clustering methods," in *Data Mining and Knowledge Discovery Handbook*, O. Maimon, L. Rokach, Eds. (Springer US, Boston, MA, 2005), pp. 321–352.
51. J. Marrison, L. Räty, P. Marriott, P. O'Toole, Ptychography—A label free, high-contrast imaging technique for live cells using quantitative phase information. *Sci. Rep.* **3**, 2369 (2013).
52. K. Benzerara *et al*., Study of the crystallographic architecture of corals at the nanoscale by scanning transmission X-ray microscopy and transmission electron microscopy. *Ultramicroscopy* **111**, 1268–1275 (2011).
53. L. C. Nielsen, D. J. DePaolo, J. J. De Yoreo, Self-consistent ion-by-ion growth model for kinetic isotopic fractionation during calcite precipitation. *Geochim. Cosmochim. Acta* **86**, 166–181 (2012).
54. B. R. Constantz, Coral skeleton construction: A physiochemically dominated process. *Palaios* **1**, 152–157 (1986).
55. B. A. Collins *et al*., Polarized X-ray scattering reveals non-crystalline orientational ordering in organic films. *Nat. Mater.* **11**, 536–543 (2012).
56. C. Donnelly *et al*., Three-dimensional magnetization structures revealed with X-ray vector nanotomography. *Nature* **547**, 328–331 (2017).
57. P. Ferrand, A. Baroni, M. Allain, V. Chamard, Quantitative imaging of anisotropic material properties with vectorial ptychography. *Opt. Lett.* **43**, 763–766 (2018).
58. T. A. Grünewald *et al*., Mapping the 3D orientation of nanocrystals and nanostructures in human bone: Indications of novel structural features. *Sci. Adv.* **6**, eaba4171 (2020).
59. Elia Beniash *et al*., The hidden structure of human enamel. *Nat. Commun.* **10**, 4383 (2019).
60. Tilman A. Grünewald *et al*., Mapping the 3D orientation of nanocrystals and nanostructures in human bone: Indications of novel structural features. *Sci. Adv.* **6**, eaba4171 (2020).
61. Vanessa Schoeppler *et al*., Crystal growth kinetics as an architectural constraint on the evolution of molluscan shells. *Proc. Natl. Acad. Sci. U.S.A.* **116**, 20388–20397 (2019).
62. Iryna Polishchuk *et al*., Coherently aligned nanoparticles within a biogenic single crystal: A biological prestressing strategy. *Science* **358**, 1294–1298 (2017).
63. M. Lerotic, R. Mak, S. Wirick, F. Meirer, C. Jacobsen, MANTiS: A program for the analysis of X-ray spectromicroscopy data. *J. Synchrotron Radiat.* **21**, 1206–1212 (2014).
64. L. Muscatine *et al*., Stable isotopes (δ13C and δ15N) of organic matrix from coral skeleton. *Proc. Natl. Acad. Sci. U.S.A.* **102**, 1525–1530 (2005).
65. A. Pryor Jr *et al*., GENFIRE: A generalized Fourier iterative reconstruction algorithm for high-resolution 3D imaging. *Sci. Rep.* **7**, 10409 (2017).
66. Y. Yang *et al*., Deciphering chemical order/disorder and material properties at the single-atom level. *Nature* **542**, 75–79 (2017).
67. J. Zhou *et al*., Observing crystal nucleation in four dimensions using atomic electron tomography. *Nature* **570**, 500–503 (2019).
68. X. Tian *et al*., Correlating the three-dimensional atomic defects and electronic properties of two-dimensional transition metal dichalcogenides. *Nat. Mater.* **19**, 867–873 (2020).
69. M. C. Scott *et al*., Electron tomography at 2.4-ångström resolution. *Nature* **483**, 444–447 (2012).
70. J. Miao, D. Sayre, H. N. Chapman, Phase retrieval from the magnitude of the Fourier transforms of nonperiodic objects. *J. Opt. Soc. Am. A Opt. Image Sci. Vis.* **15**, 1662–1669 (1998).